Hyperspectral Image Denoising via Low-Rank Representation and CNN Denoiser

Hezhi Sun, Ming Liu, Ke Zheng, Dong Yang, Jindong Li, and Lianru Gao, *Senior Member, IEEE*

***Abstract*—Hyperspectral images (HSIs) are widely used in various tasks such as earth observation and target detection. However, during the imaging process, HSIs are often corrupted by various noises. In this article, we firstly investigate the advantages of traditional physical restoration models and the denoising convolutional neural networks (CNN) for HSIs denoising tasks. The sparse based low-rank representation can explore the global correlations in both the spatial and spectral domains, and the CNN-based denoiser can represent the deep prior which cannot be designed by traditional restoration models. Then, we propose a HSI denoising model with low-rank representation and CNN denoiser prior in the flexible and extensible plug-and-play framework by combining the advantages of the two methods. The proposed model is user-friendly, requiring no retraining. Simulated data experiments show that, compared with competitive methods, the proposed one achieves better denoising results for both additive Gaussian noise and Poissonian noise in various quantitative evaluation indicators. Real data experiments show that the proposed model yields the best performance.**

***Index Terms*—Convolutional neural network (CNN), hyperspectral image (HSI) denoising, low-rank representation.**

I. INTRODUCTION

REMOTE sensing imaging is the technology that uses satellites, airplanes and other spacecraft carrying imaging equipment to observe the ground object. Through the propagation and reception of electromagnetic waves, it perceives the characteristics of ground objects and has the advantages of large-scale observation and freedom from geographical restrictions. It can simultaneously obtain spatial and spectral information of the ground object [1], [2].

Hyperspectral images (HSIs) provide hundreds of continuous observation bands throughout the electromagnetic spectrum from the visible to the near-infrared wavelength ranges. With the high-dimensional and distinguishing spectral features, hyperspectral remote sensing technology has been widely used in various fields, such as earth observation, environmental protection, and natural disaster monitoring [3]–[6]. However, due to various factors, such as thermal electronics, dark current, random errors in light counting and other factors in the imaging process, HSIs will inevitably be affected by noises, such as such as Gaussian noise, stripes, deadlines, and impulse noise. Therefore, HSI denoising, as a pre-processing step for subsequent applications, is an important research direction that has attracted much attention in recent decades [7].

Existing HSIs denoising methods can be categorized into two groups: spatial based method and spectral-spatial based method. From the perspective of human vision, the former treats each band of the HSI as a grayscale image, and directly applies the mature denoising algorithm for grayscale image or RGB image to the HSI, denoising band by band. Representative examples of this type of methods include nonlocal mean (NLM) [8], total variation (TV) [9], Gaussian mixture model (GMM) [10], weighted nuclear norm minimization (WNNM) [11] and the collaborative filtering of groups of similar patches block-matching and three-dimensional filtering (BM3D) [12]. This type of methods focuses on denoising from the spatial dimension, and mainly utilizes the self-similar characteristics of the images. However, the information of the spatial dimension cannot fully reflect all the information of the HSI, and it ignores the high correlation between the bands of the HSI.

The spectral-spatial based methods consider the spectral information on the basis of the spatial-based method and could make full use of the high correlation in the spatial dimension and the spectral dimension of HSIs [13]. For example, the spectral-spatial adaptive hyperspectral TV [14] could adaptively adjust the noise reduction intensity of each pixel according to different types of features in the spatial domain, simultaneously, the algorithm could also adjust the noise reduction intensity of each band according to the noise intensity of different bands; BM4D [15] and VBM4D [16] which are based on the BM3D algorithm, use collaborative filtering in 3-D patches extracted from image sequences and videos, respectively; MSPCA-BM3D [17] is to denoise based on nonlocal spatial adaptation and spectral dimension decorrelation for multispectral or HSIs; multichannel WNNM method [18] expands the gray image denoising model (WNNM) to RGB image denoising by introducing a weighting matrix; PCA+BM4D [19] first performs the principal component analysis (PCA) transformation on the noisy HSIs, keeping the high-energy principal components of the first few signals unchanged, and uses the BM4D to denoise for the low-energy principal components of the remaining signal.

Manuscript received October 23, 2021; revised December 15, 2021; accepted December 22, 2021. Date of publication December 28, 2021; date of current version January 7, 2022. This work was supported in part by the National Natural Science Foundation of China under Grant 61833009 and Grant 61690212 and in part by the Heilongjiang Touyan Team and China Postdoctoral Science Foundation under Grant 2021M693234. *(Corresponding author: Ming Liu.)*

Hezhi Sun and Ming Liu are with the Research Center of Satellite Technology, Harbin Institute of Technology, Harbin 150001, China (e-mail: sunhezhi@hotmail.com; mingliu23@hit.edu.cn).

Ke Zheng and Lianru Gao are with the Key Laboratory of Digital Earth Science, Aerospace Information Research Institute, Chinese Academy of Sciences, Beijing 100094, China (e-mail: zhengkevic@aircas.ac.cn; gaolr@aircas.ac.cn).

Dong Yang and Jindong Li are with the Chinese Academy of Sciences, Beijing 100094, China (e-mail: qbdyzy@sina.com; ljdcast@163.com).

Digital Object Identifier 10.1109/JSTARS.2021.3138564

With the vigorous development of compressed sensing theory, the low-rank representation of high-dimensional data has attracted more and more attention [20]. The high correlation in the spatial and spectral dimensions of HSIs makes it exhibit low-rank characteristics. More and more HSI processing algorithms based on low-rank representation have been proposed, for example, LRCF [21], NAILRMA [22], LRTV [23], FastHyDe [24], RhyDe [25], WLRTR [26], FLLRSC [27], LSDM-MoG [28], etc.

Recent years, deep learning-based models have been introduced for nature images and HSIs applications [29]–[35]. The spatial-spectral features can be extracted by deep convolutional neural network, and these features represent low-to-high level semantic information, and that denoising, destriping and super-resolution are classical low-level vision tasks. Convolutional neural network-based DnCNN [36] and FFDNet [37] are two representative deep-denoising methods for single image, which show good results. For HSIs denoising task, HSI-DeNet [35] and spatial-spectral gradient network (SSGN) [38] show impressive results. Due to the end-to-end training, the learning-based method is not only faster in testing, but also has better performance. In contrast, traditional (model-based) methods are usually time-consuming with complex priors to achieve good performance. Taking into account their respective merits and drawbacks, it is natural to think of integrating the two together to take advantage of their respective merits. This integration leads to a deep plug-and-play (PnP) [39] HSI denoising method, which uses a learning-based CNN denoiser prior to replace that in model-based method.

In this article, we resort to the PnP framework to address HSI denoising task. A low-rank and sparse representation method is used to model the spatial–spectral low-rank prior of HSIs and derive orthogonal subspace representation coefficients images (herein termed eigen-images), while eigen-images are denoised with the CNN-based DRUNet [40]. We embed them both into the PnP framework to propose a PnP HSI denoising model with low-rank representation and CNN denoiser prior. One can find the flowchart of our model in Fig. 1. In the proposed PnP framework, the submodel of low-rank based orthogonal subspace representation refers to [24], the eigen-images are denoised by the submodel of DRUNet.

The contribution of this article is summarized as follows.

1) A novel framework for HSIs denoising called PnP HSI denoising model with low-rank representation and CNN denoiser prior is proposed. Compared with the traditional HSI denoising methods and other PnP-based denoising frameworks, the proposed model is more universal, requiring no retraining.
2) The framework combines traditional methods and deep learning methods. On the one hand, it uses a low-rank representation framework to make full use of the spatial and spectral information of HSIs. On the other hand, it uses the intensity fitting and computing power of deep learning to improve the generalization of the algorithm.

The rest of this article is organized as follows: Section II introduces related works, including PnP framework, low-rank representation, and denoising CNN. Section III presents the details of the PnP HSI denoising model. Section IV evaluates the performances of our method compared with those of other hyperspectral denoisers. Finally, Section V concludes this article.

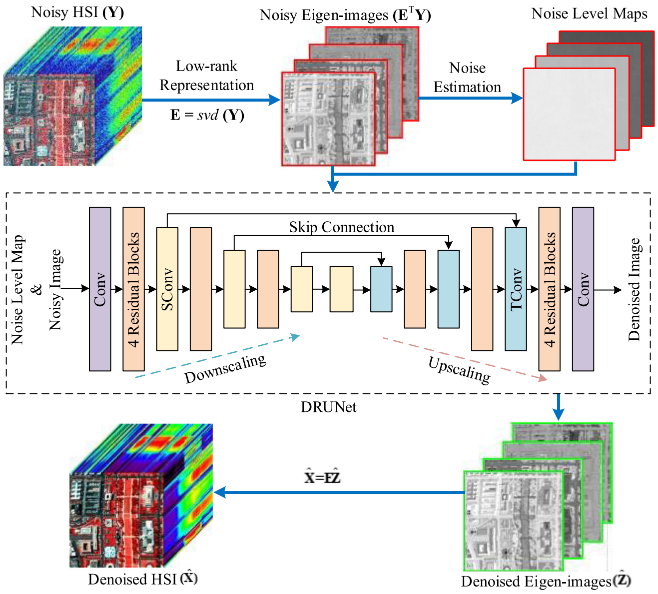

Fig. 1. Flowchart of the proposed method. It includes three stages: A Low-rank representation to get Eigen-images; B. Eigen-images denoising by DRUNet; and C. Inverse transformation to get denoised HSI. PnP is a bridge connecting A, B, and C.

II. Related Works

In this section, we briefly review and discuss the three major categories of relevant work, which are low-rank and sparse characteristic of HSIs, PnP framework and denoising CNN.

A. *Low-Rank and Sparse Characteristic of HSIs*

The column rank of a matrix is the maximum number of linearly independent columns, and the row rank is the maximum number of linearly independent rows. The row rank and column rank of a matrix are always equal, which can be simply called the rank of the matrix. The less nonzero elements in the singular values of the matrix, the lower the rank of the matrix is. In the field of information processing, rank represents the redundancy of information. The lower the rank, the higher the redundancy of information.

Like natural images, the information of each band of HSI represents the reflectivity of the same object in different spectrums, the image of each band has self-similar characteristics, so there is correlation between different pixels. Similarly, in the spectral dimension, due to the narrow interval between adjacent bands, there is even a certain spectral overlap, so that there is high correlation between adjacent and even nonadjacent bands. The high correlation in the spatial and spectral dimensions of HSI makes it exhibit low-rank and sparse characteristics. However, the noise will weaken the correlation in the spatial dimension and the spectral dimension of HSI, and accordingly increases the rank of the image matrix. Taking the Washington dc scene

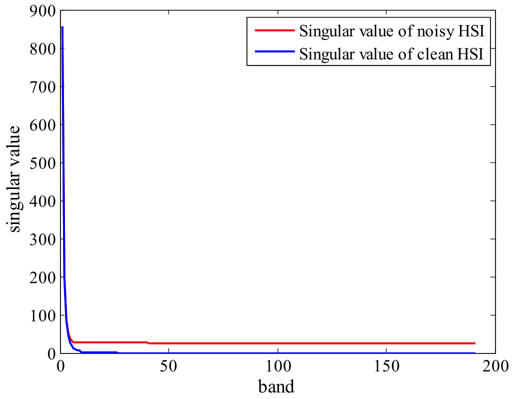

Fig. 2. Singular value of Washington dc subscene disturbed by noise.

disturbed by noise as an example, Fig. 2 intuitively describes this process. The singular value curves are obtained by singular value decomposition (SVD) on image matrix of HSI. The larger singular value determines the “main feature” of the image, that is, the main signal energy of the HSI. It can be seen that the singular values of image matrix of clean HSI are almost close to 0 after the eighth band, while the singular values of the image matrix of HSI disturbed by noise are obviously higher than 0. The smaller singular values after the 8th band are caused by noise, and the presence of noise increases the rank of the image matrix. Although the presence of noise weakens the correlation in the spatial and spectral dimensions of HSI, there is still a lot of redundancy in the images. Simultaneously, research [41] shows that in most real observation scenarios, although the observed HSI is interfered by noise, there is still high correlation between the spectral vectors.

B. Plug-and-Play Framework

Recently, some works [42]–[45] using PnP framework for HSI processing have been proposed. The main idea of PnP is that it can decouple complex objective function through a certain variable splitting algorithm into several related submodels, except for the input and output each submodels can be flexibly replaced with other similar models [46]. For image restoration (IR), first, the data item and the prior item of the objective function are decoupled through a certain variable splitting algorithm, such as alternating direction method of multipliers [47] and half-quadratic splitting [48], so as to obtain an iterative scheme consisting of alternately solving the data subproblem and the prior subproblem. Then we can use any available denoiser to solve the prior subproblem, such as NLM [8], GMM [10], and BM3D [12].

For PnP IR, the denoising operators are basically divided into two categories: one is the traditional model-based denoiser, and the other is the deep CNN denoiser. For example, some research using the BM3D, GMM, or WNNM denoiser prior in a PnP framework for image deblurring [49]–[52], super-resolution [53], and denoising [24], [54]. These methods decouple the data term and regularization term, then the regularization prior is implicitly defined via the flexible denoisers, unlike traditional model-based methods which need to specify the explicit and handcrafted image priors.

CNN-based denoising methods have achieved efficient and effective results, with the development of deep learning. Therefore, some CNN-based PnP IR methods [55]–[59] have been proposed, mainly taking IRCNN or DnCNN as denoiser. These methods either adopt multiple CNN denoisers trained for different noise levels to cover a wide range of noise levels or use a single denoiser trained on a certain noise level, which are not suitable to solve the denoising subproblem [40]. For example, IRCNN denoiser consists of 25 separate 7-layer denoisers, among which each denoiser is trained on an interval noise level of 2 [56]. This undoubtedly increases the number of iterations, calculation amount and affects the performance.

C. Denoising CNN

As we introduced earlier, convolutional neural network-based DnCNN [36] and FFDNet [37] are two representative deep-denoising methods for single image. The main improvement of DnCNN includes: adding batch norm-alization; and the strategy of residual learning is introduced, unlike previous networks that learn clean images from noisy images, DnCNN learns the distribution of noise from noisy images to obtain residual image, then makes difference between the residual image and the original image to get the denoised image. This residual learning strategy greatly reduces the amount of the network parameters. DnCNN has achieved a good denoising effect on both independent and identically distributed (i.i.d.) Gaussian noise and non-independent and identically distributed (Non-i.i.d.) Gaussian noise. However, it has limited effect on real image denoising. FFDNet is based on DnCNN and uses a noise level map as input, so that the network can handle a wide range of noise levels.

For HSI denoising, HSI-DeNet [35] and SSGN [38] are two representative deep denoisers, showing impressive results. When the network is properly trained, the deep denoiser will be much faster than the denoiser based on traditional machine learning. However, the denoising performance is highly dependent on the training data.

The abovementioned denoisers are difficult to directly meet the requirement of the proposed PnP HSI denoising framework, that is, single image denoising, blind denoising and handling a wide range of noise levels via a single model. Perhaps the most suitable denoiser for PnP denoising is FFDNet, but its performance is only comparable to DnCNN and IRCNN, thus it may not be able to improve the performance of PnP denoising. In response to above problems, Zhang *et al.* [40] proposed a flexible and powerful denoiser called DRUNet which combined U-Net and ResNet. DRUNet takes the noise level map as input and has the ability to handle various noise levels via a single model. Compared with FFDNet and IRCNN, DRUNet has better performance. Moreover, even trained on noise level range of [0, 50], DRUNet can still perform well on an extremely large unseen noise level of 200. Therefore, it is perfectly suitable for PnP IR task.

III. FORMULATION AND PROPOSED METHOD

In this section, we described the HSI denoising problem formulation first and then a generality framework called PnP

HSI denoising model with low-rank representation and CNN denoiser prior was proposed.

A. Problem Formulation

The clean 2-D matrix of HSI $\boldsymbol{X} = [\boldsymbol{x}_1, \ldots, \boldsymbol{x}_n] \in \mathbb{R}^{n_b \times n}$ (n_b is the number of bands, n is the size of spectral vector in $\boldsymbol{X}$) is degraded by the interference of additive Gaussian noise. Therefore, the observation model of HSI can be expressed as

$$\boldsymbol{Y} = \boldsymbol{X} + \boldsymbol{N} \tag{1}$$

where $\boldsymbol{Y}, \boldsymbol{N} \in \mathbb{R}^{n_b \times n}$, $\boldsymbol{N}$ is the additive Gaussian noise. The algorithm solution model can be expressed as

$$\min_{\boldsymbol{X}} \frac{1}{2} \|\boldsymbol{Y} - \boldsymbol{X}\|_F^2 + \tau \mathrm{rank}(\boldsymbol{X}) \tag{2}$$

where $\boldsymbol{X}_F^2 = \mathrm{trace}(\boldsymbol{X}\boldsymbol{X}^T)$ is the Frobenius norm of $\boldsymbol{X}$, τ is a positive regularization parameter to balance the two terms. Equation (2) is nonconvex and has no effective solution. To find an effective solution, we replace $\mathrm{rank}(\boldsymbol{X})$ with the nuclear norm $\|\boldsymbol{X}\|_* = \sum_i \sigma_i (\boldsymbol{X})$ of $\boldsymbol{X}$, and $\sigma_i(\boldsymbol{X})$ represents the *i*th singular value of $\boldsymbol{X}$. Thus, the transformed convex optimization model can be expressed as

$$\min_{\boldsymbol{X}} \frac{1}{2} \|\boldsymbol{Y} - \boldsymbol{X}\|_F^2 + \tau \|\boldsymbol{X}\|_*. \tag{3}$$

B. PnP HSI Denoising Model

A low-rank and sparse representation method is used to model the spatial–spectral low-rank prior of HSIs and derive eigen-images, while the eigen-images are denoised with DRUNet. We embed them both into the PnP framework to propose the PnP HSI denoising model. It is mainly composed of three steps: low-rank representation of HSI, eigen-images denoising by DRUNet and inverse transformation to get denoised HSI.

Step 1: Low-Rank Representation of HSI: For additive Gaussian i.i.d. noise, the transformed convex optimization model is as Equation (3).

As we introduced in Related Works, although the presence of noise weakens the correlation in the spatial and spectral dimensions of HSI, there is still a lot of redundancy in the images. In most real observation scenarios, although the observed HSI is interfered by noise, there is still high correlation between the spectral vectors. Therefore, $\boldsymbol{x}_i, i = 1, \ldots, n$ live in a low-dimensional orthogonal subspace S_p, with $p \ll n_b$. From the perspective of low-rank representation, $\boldsymbol{X}$ can be expressed as a linear combination of an orthogonal base matrix $\boldsymbol{E} = [\boldsymbol{e}_1, \ldots, e_p] \in \mathbb{R}^{n_b \times p}$ and a corresponding representation coefficient matrix $\boldsymbol{Z} = [z_1, \ldots, z_n] \in \mathbb{R}^{p \times n}$,

$$\boldsymbol{X} = \boldsymbol{E}\boldsymbol{Z}. \tag{4}$$

In real observation scene, the two-dimensional matrix $\boldsymbol{X}$ of the clean HSI is unknown. Therefore, an effective and feasible method is needed to learn the orthogonal base matrix $\boldsymbol{E}$ from the observed two-dimensional matrix $\boldsymbol{Y}$ of the noisy HSI. $\boldsymbol{E}$ can be learned using HySime algorithm [60] or SVD. As we mentioned earlier, the images associated with the rows of $\boldsymbol{Z}$ are called as eigen-images. It can be seen from (5) that the eigen-images are linear representations of the original images ($\boldsymbol{x}_i, i = 1, \ldots, n$). Therefore, in the process of projecting the original HSI into the low-dimensional orthogonal subspace, the self-similar in spatial structure is not destroyed, so the eigen- images also have the self-similar characteristics [24].

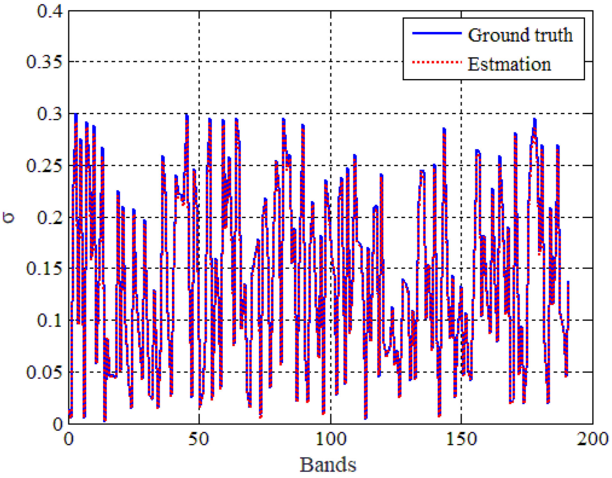

Fig. 3. Gaussian noise level σ of Washington DC Mall subscene disturbed by Gaussian non-i.i.d. noise. Blue line denotes the ground truth and red one denotes the estimated noise level.

Step 2: Eigen-Images Denoising With DRUNet: Referring to [24], the components of $\boldsymbol{Z}$ which are the eigen-images tend to be decorrelated. Regularization operator $\phi(\boldsymbol{Z})$ can be expressed as

$$\phi\left(\boldsymbol{E}^T\boldsymbol{Y}\right) = \begin{bmatrix} \phi\left(\boldsymbol{e}_1^T\boldsymbol{Y}\right) \\ \vdots \\ \phi\left(\boldsymbol{e}_p^T\,\boldsymbol{Y}\right) \end{bmatrix}. \tag{5}$$

The eigen-images denoising problem can be formulated as

$$\begin{aligned} \hat{\boldsymbol{Z}} &= \arg\min_{\boldsymbol{Z}} \frac{1}{2} ||\boldsymbol{E}\boldsymbol{Z} - \boldsymbol{Y}||_F^2 + \lambda\phi(\boldsymbol{Z}) \\ &= \arg\min_{\boldsymbol{Z}} \frac{1}{2} \left\|\boldsymbol{Z} - \boldsymbol{E}^T\right\| \boldsymbol{Y}_F^2 + \lambda\phi(\boldsymbol{Z}). \end{aligned} \tag{6}$$

We resort to the PnP prior framework to address the denoising problem, the proposed method uses DRUNet as regularization denoiser to denoising the eigen-images band by band. Therefore, $\phi(\cdot)$ denotes the network of DRUNet, the input are noisy eigen-images and output are corresponding denoised ones. As we mentioned in the related works, DRUNet is a flexible and powerful denoiser, which could handle images with various noise levels without retraining the network. Not mention that it is much faster than other machine learning-based denoisers. It should be noted that DRUNet takes the noisy images and corresponding level maps as input, the noise level map is a uniform map filled with noise level σ and has the same spatial size as noisy images. Here, we refer to [60] to do the noise level estimation. In order to verify the accuracy of the estimation method, the different variance zero-mean Gaussian noise (Gaussian non-i.i.d. noise) is added to each band of Washington DC Mall subscene, with σ being randomly selected from 0 to 0.3. Fig. 3 shows the truth noise levels and estimated ones.

Step 3: Inverse Transformation to Denoised HSI: After eigen-images denoising, the denoised HSI can be written as

$$\hat{\boldsymbol{X}} = \boldsymbol{E}\hat{\boldsymbol{Z}}. \tag{7}$$

For additive Gaussian non-i.i.d. noise, that is, when the Gaussian noise intensity of each band is different, the HSI $\boldsymbol{Y}$ should be Gaussian whitening before eigen-images denoising, so the Gaussian non-i.i.d. noise will be transformed into Gaussian i.i.d. noise. For poissonian noise, the Anscombe transform will be applied to converts Poissonian noise into approximately additive noise [24].

IV. EXPERIMENTS

To verify the effectiveness of our model, lots of experiments on simulation and real HSI data are conducted. Five different denoising methods, classic BM3D [12], DRUNet [40], HSID-CNN [61], NAILRMA [22], and FastHyDe [24] are selected as comparison methods, besides that for comparison we take DnCNN as denoising submodel to replace DRUNet in the proposed framework. It should be noted that DRUNet and DnCNN with pre-trained model parameters are used in the experiment. For HSID-CNN, we have retrained the network with the same settings and datasets in [61]. The parameters of all comparison methods are the optimal parameters given in their original literature. For our method, the spectral vectors in the two datasets are projected on an orthogonal signal subspace learned via Hysime.

Experiment Environment. The algorithms were implemented on MATLAB R2014a and Pytorch framework on a desktop PC equipped with Intel Core i7-6700 CPU (at 3.60 GHz), NVIDIA Titan Xp GPU and 16 GB of RAM memory.

A. Simulated Data Experiments

Two HSIs are used to evaluate the performance of the proposed model including: Washington DC Mall subscene and Pavia Centre subscene.

1) *Washington DC Mall:* This data was taken by HYDICE sensor in Washing DC Mall. The wavelength range is 400–2500 nm. To simulate the clean images, low signal-to-noise bands, due to the water vapor absorption, were discarded, and 191 bands were remained. The ground sample distance (GSD) of this data is 2.8 m and the image size selected in the experiment is 256 × 256 pixels.
2) *Pavia Centre:* The second data was gathered by ROSIS sensor using flight campaign in Pavia. It contains pixels with 115 spectral bands from 430–860 nm. Because the atmospheric absorption affection, 80 spectral bands were remained with 35 bands discarded. The GSD of this data is 1.3 m. The image size selected in the experiment is 200×200 pixels.

Before adding simulated noise, the gray values of HSIs are normalized to [0, 1] band by band, and they are restored to the original interval after denoising. For comparison, we use the similar experiment settings as [24] to generate noisy HSI data under there different noise cases. The details are listed in the following.

1) *Case 1:* In this case, the noise intensity was equal for different bands. Zero-mean Gaussian noise of same variances (Gaussian i.i.d. noise) was added to each band. The variances of the Gaussian noise are $\{0.02^2\ 0.04^2\ 0.06^2\ 0.08^2\ 0.1^2\ 0.2^2\ 0.3^2\}$.
2) *Case 2:* In this case, the noise intensity was different for different bands. That is, different variance zero-mean Gaussian noise (Gaussian non-i.i.d. noise) was added to each band, with the variance value being randomly selected from 0 to 0.1^2.
3) *Case 3:* In this case, Poissonian noise $\boldsymbol{Y} \sim P(\alpha \boldsymbol{X})$ was added, where $\mathrm{P(A)}$ stands for a matrix of size(A) of independent Poisson random variables whose parameters are given by the corresponding element of $\mathrm{A} := [a_{ij}]$. The parameter α is such that $\mathrm{SNR} := \alpha(\sum i, ja_{ij}{}^2)/(\sum i, ja_{ij})$ was set 15 dB.

For data in case 3, the Poissonian noise is converted into approximately additive noise by applying the Ansocmbe transform $\tilde{\boldsymbol{Y}} := 2\sqrt{\boldsymbol{Y} + \frac{3}{8}}$, since the compared methods assume additive Gaussian noise.

The peak signal-to-noise (PSNR) index and the structural similarity (SSIM) index of each band are calculated for quantitative assessment. The larger the PSNR and SSIM, the better the restoration performance of the corresponding method. The corresponding mean PSNRs (MPSNR) and mean SSIMs (MSSIM) for Washington DC Mall data and for Pavia Centre are reported in Tables I and II, respectively. In all cases our model achieves the best results compared with other methods and the gains increase as the noise increases. It is worth noting that our model achieves an improvement of MSSIM more than 0.5 dB compared with the second-best result.

For visual evaluation, we show the 70th band of the recovered HSI with the noise in case 1 (the variance of the Gaussian noise is 0.1^2), cases 2 and 3 in Figs. 4 and 5, it can be seen that the results of our model are closest to the original reference images comparing with other methods, especially in the preservation of details. The reconstructed spectral vectors for different denoising methods in all cases are depicted in Figs. 6 and 7, it is also clear from the results of our model that the spectral characteristics are closest to ones in the clean HSI. Figs. 8 and 9 show the PSNR and SSIM values of each band of denoised Washington DC Mall data and Pavia data, our proposed method shown in red, uniformly provides the best performances in almost all cases.

From the comparison with results of FastHyDe and Suspace + DnCNN, it can be seen that DRUNet is more suitable for the eigen-images denoising in this framework than BM3D and DnCNN. Our model takes advantage of CNN denoiser and traditional low-rank representation method.

B. Real Data Experiments

To further verify the effectiveness of the proposed denoising method, two real-world data, the AVIRIS (airborne visible/infrared imaging spectrometer) Indian Pines scene and GF-5 data, were employed in our real data experiments.

1) *Indian Pines:* This image recorded over North-western Indiana of 20 m per pixel and 220 spectral channels. The size of the selected scene is 145 × 145 pixels, with strong noise in a few bands.

TABLE I
QUANTITATIVE ASSESSMENT OF DIFFERENT ALGORITHMS APPLIED TO WASHINGTON DC MALL

	σ	Index	Noisy Image	BM3D	DRUNet	HSID-CNN	NAILRMA	FastHyDe	Subspace+DnCNN	Ours
Case 1	0.02	MPSNR	33.98	36.31	37.15	42.51	48.38	49.69	48.46	**50.14**
		MSSIM	0.9370	0.9667	0.9727	0.9928	0.9977	0.9981	0.9976	**0.9983**
	0.04	MPSNR	27.96	32.03	32.89	38.29	43.14	44.78	44.50	**45.32**
		MSSIM	0.8099	0.9164	0.9319	0.9813	0.9921	0.9945	0.9942	**0.9952**
	0.06	MPSNR	22.44	29.82	30.64	35.17	40.24	41.97	41.93	**42.54**
		MSSIM	0.6824	0.8667	0.8909	0.9651	0.9835	0.9901	0.9900	**0.9914**
	0.08	MPSNR	21.94	28.37	29.15	33.39	38.20	40.09	40.16	**40.72**
		MSSIM	0.5728	0.8207	0.8523	0.9475	0.9760	0.9853	0.9855	**0.9873**
	0.1	MPSNR	19.99	27.31	28.05	34.26	36.69	38.69	38.82	**39.39**
		MSSIM	0.4832	0.7786	0.8164	0.9505	0.9680	0.9804	0.9808	**0.9832**
	0.2	MPSNR	13.98	24.23	24.98	30.26	31.73	34.50	34.76	**35.26**
		MSSIM	0.2288	0.6067	0.6719	0.8973	0.9192	0.9542	0.9562	**0.9611**
	0.3	MPSNR	10.46	22.75	23.45	27.55	28.98	32.25	32.55	**33.01**
		MSSIM	0.1282	0.5048	0.5731	0.8257	0.8647	0.9282	0.9313	**0.9382**
Case 2		MPSNR	28.62	32.99	33.76	38.91	47.44	51.29	49.16	**51.52**
		MSSIM	0.7507	0.8928	0.9118	0.9788	0.9977	0.9983	0.9978	**0.9984**
Case 3		MPSNR	26.98	31.33	32.15	37.04	41.78	43.21	43.21	**43.75**
		MSSIM	0.7980	0.9129	0.9250	0.9731	0.9881	0.9914	0.9920	**0.9931**

TABLE II
QUANTITATIVE ASSESSMENT OF DIFFERENT ALGORITHMS APPLIED TO PAVIA CENTRE DATA

	σ	Index	Noisy Image	BM3D	DRUNet	HSID-CNN	NAILRMA	FastHyDe	Subspace+DnCNN	Ours
Case 1	0.02	MPSNR	33.98	36.75	37.66	42.84	46.67	46.98	46.01	**47.41**
		MSSIM	0.9330	0.9670	0.9731	0.9924	0.9952	0.9965	0.9956	**0.9968**
	0.04	MPSNR	27.97	32.78	33.69	38.44	41.70	42.54	42.40	**43.09**
		MSSIM	0.7948	0.9224	0.9369	0.9789	0.9870	0.9908	0.9903	**0.9919**
	0.06	MPSNR	24.43	30.64	31.51	35.57	38.86	40.02	40.01	**40.66**
		MSSIM	0.6548	0.8784	0.9000	0.9631	0.9775	0.9841	0.9839	**0.9863**
	0.08	MPSNR	21.94	29.20	30.02	33.93	36.80	38.33	38.39	**39.06**
		MSSIM	0.5372	0.8372	0.8645	0.9417	0.9646	0.9770	0.9773	**0.9807**
	0.1	MPSNR	19.99	28.12	28.90	34.61	35.29	36.98	37.11	**37.78**
		MSSIM	0.4408	0.7991	0.8309	0.9506	0.9540	0.9698	0.9705	**0.9749**
	0.2	MPSNR	13.98	24.93	25.65	30.69	30.43	33.33	33.66	**34.27**
		MSSIM	0.1897	0.6349	0.6899	0.8940	0.8811	0.9361	0.9396	**0.9472**
	0.3	MPSNR	10.46	23.35	23.96	27.72	27.58	31.33	31.64	**32.27**
		MSSIM	0.1029	0.5255	0.5850	0.8069	0.8008	0.9045	0.9093	**0.9205**
Case 2		MPSNR	28.73	33.81	34.60	40.19	43.49	48.59	46.52	**48.87**
		MSSIM	0.7204	0.8990	0.9163	0.9829	0.9935	0.9977	0.9964	**0.9978**
Case 3		MPSNR	26.97	32.25	32.70	37.14	40.59	41.63	41.61	**42.14**
		MSSIM	0.7592	0.9125	0.9263	0.9700	0.9848	0.9891	0.9888	**0.9904**

TABLE III
AVERAGE RUNTIME COMPARISONS FOR HSI DENOISING METHODS IN REAL EXPERIMENTS

Method	BM3D	DRUNet	HSID-CNN	NAILRMA	FastHyDe	Sub+DnCNN	Ours
Time (s)	53	17	3	15	10	4	5

The noise was assumed to be non-i.i.d. and estimated with HySime. The subspace dimension input to our model and FastHyDe is set to 25, considering the robustness of FastHyDe to subspace dimension overestimation [24]. Fig. 10 shows three bands of the denoised results of Indian pines (1, 2, and 61), the first column shows the noise bands, the last column shows the results of our model which yield the best performance.

The corresponding computational times are given in Table III . Qualitatively, though HSID-CNN has the shortest runtime, our method yields the best result in the second shortest

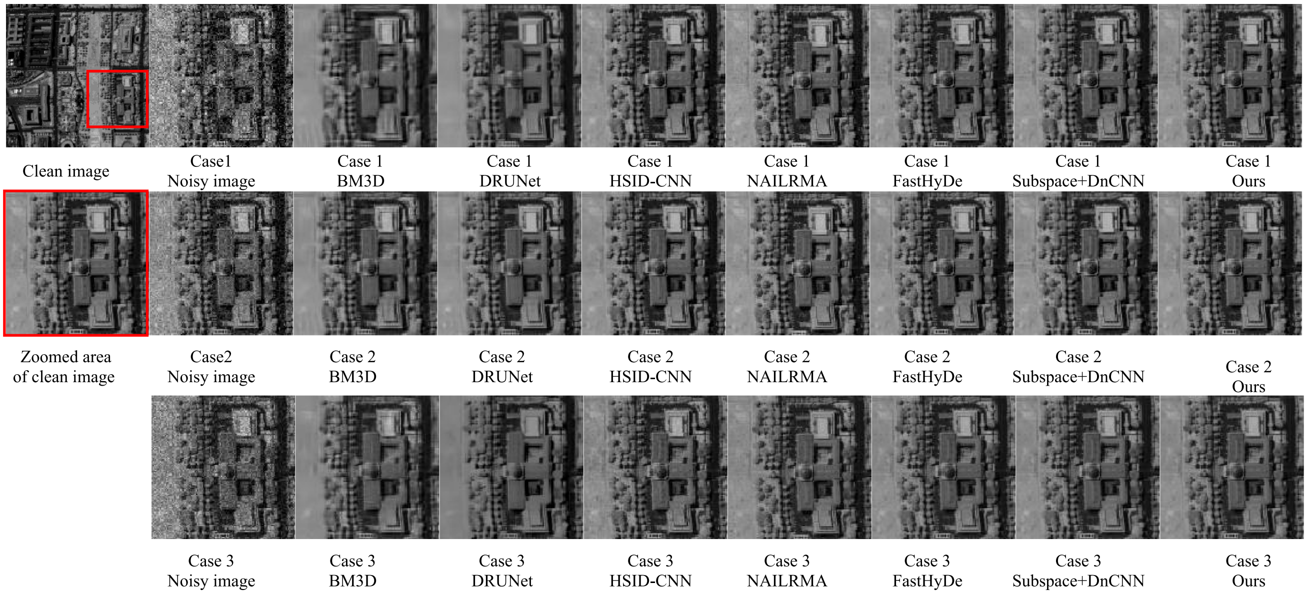

Fig. 4. Denoising result of band 70 of Washington dc dataset. Case 1: Gaussian i.i.d. $\sigma = 0.1$. Case 2: Gaussian non-i.i.d. noise. Case 3: Poissonian noise.

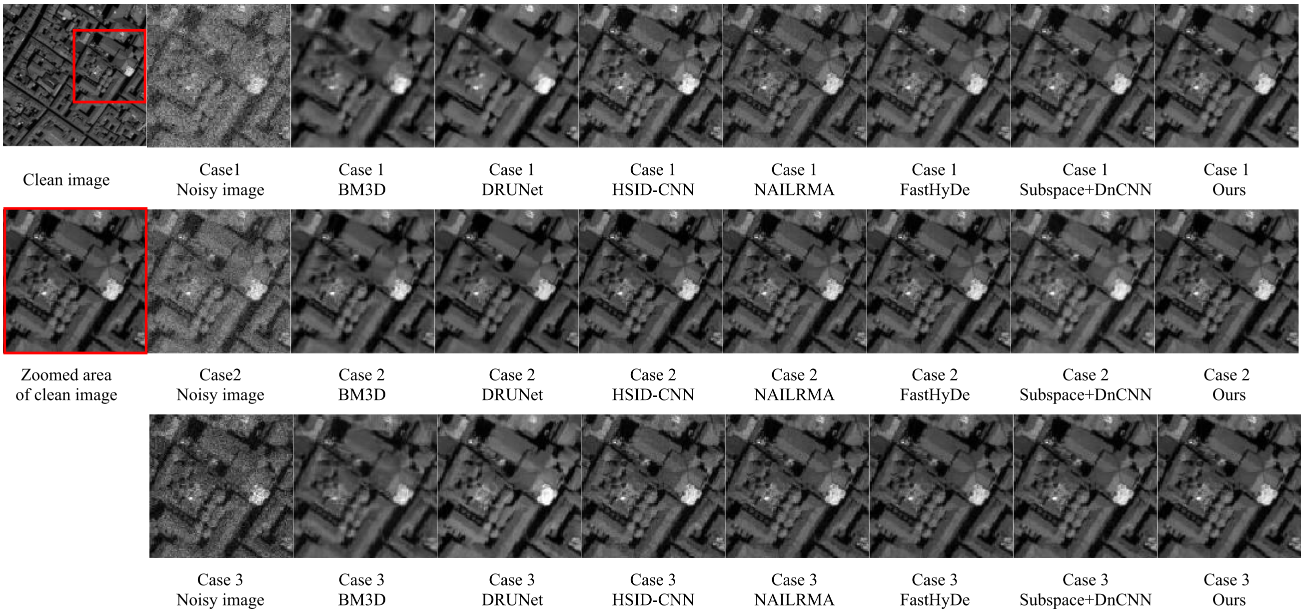

Fig. 5. Denoising result of band 70 of Pavia centre dataset. Case 1: Gaussian i.i.d. $\sigma = 0.1$. Case 2: Gaussian non-i.i.d. noise. Case 3: Poissonian noise.

time. It should be noted that steps 1 and 3 of our method is running on MATLAB, step 2 is running on Pytorch, so the calculational time of which is calculated separately and added together. Nevertheless, our method is still much faster than FastHyDe.

To further verify the effectiveness of the algorithms, we use a random forest (RF) classifier [62] to classify the HSIs before and after denoising by all comparing algorithms. The overall accuracy (OA) and the kappa coefficient are given as evaluation indexes. A total of 16 ground-truth classes were employed for testing the classification accuracy. The training sets included 10% of the test samples randomly generated from each class. Fig. 11 shows the results for Indian pines using RF classifier, and the classification accuracy results are given in Table IV. Our method produces a better classification result, with the highest OA and kappa values of 80.86% and 0.7798, respectively.

2) *GF-5 Data*: This data was acquired over an area of Fujian Province, China in January 2020, by advanced hyperspectral imager loaded by GF-5 satellite. It provides 330-bands visible/near-infrared and shortwave infrared data, covering from 400 to 2500 nm. Because the atmospheric absorption affection, 313 spectral bands were remained

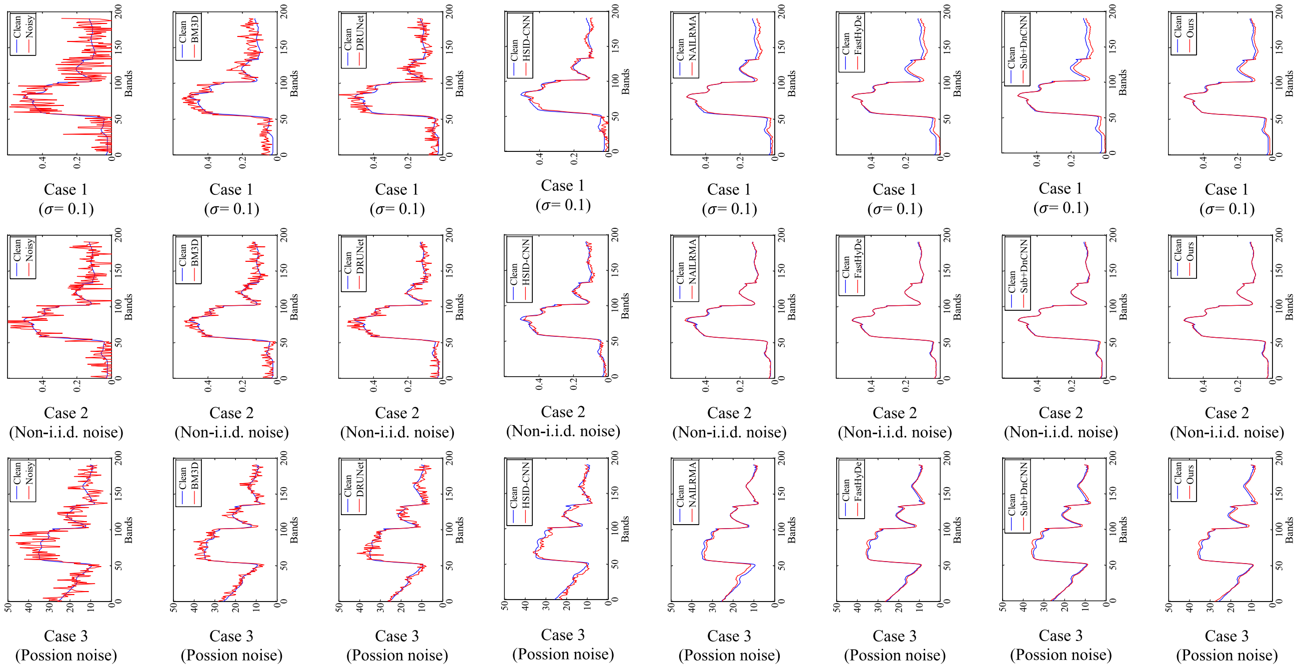

Case 1 (σ= 0.1) | Case 1 (σ= 0.1) | Case 1 (σ= 0.1) | Case 1 (σ= 0.1) | Case 1 (σ= 0.1) | Case 1 (σ= 0.1) | Case 1 (σ= 0.1) | Case 1 (σ= 0.1)

Case 2 (Non-i.i.d. noise) | Case 2 (Non-i.i.d. noise) | Case 2 (Non-i.i.d. noise) | Case 2 (Non-i.i.d. noise) | Case 2 (Non-i.i.d. noise) | Case 2 (Non-i.i.d. noise) | Case 2 (Non-i.i.d. noise) | Case 2 (Non-i.i.d. noise)

Case 3 (Possion noise) | Case 3 (Possion noise) | Case 3 (Possion noise) | Case 3 (Possion noise) | Case 3 (Possion noise) | Case 3 (Possion noise) | Case 3 (Possion noise) | Case 3 (Possion noise)

Fig. 6. Spectral vector of one pixel and its denoising results in dc Mall dataset. Case 1: Gaussian i.i.d. noise $\sigma = 0.1$. Case 2: Gaussian non-i.i.d. noise. Case 3: Poissonian noise.

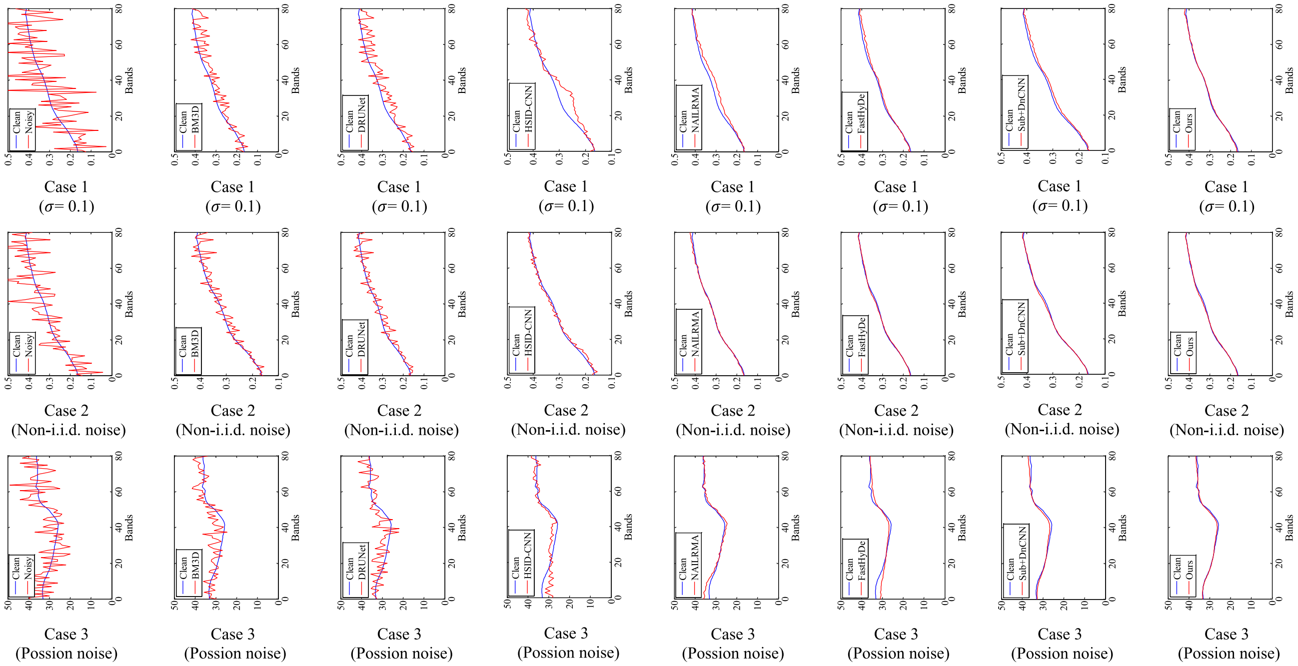

Case 1 (σ= 0.1) | Case 1 (σ= 0.1) | Case 1 (σ= 0.1) | Case 1 (σ= 0.1) | Case 1 (σ= 0.1) | Case 1 (σ= 0.1) | Case 1 (σ= 0.1) | Case 1 (σ= 0.1)

Case 2 (Non-i.i.d. noise) | Case 2 (Non-i.i.d. noise) | Case 2 (Non-i.i.d. noise) | Case 2 (Non-i.i.d. noise) | Case 2 (Non-i.i.d. noise) | Case 2 (Non-i.i.d. noise) | Case 2 (Non-i.i.d. noise) | Case 2 (Non-i.i.d. noise)

Case 3 (Possion noise) | Case 3 (Possion noise) | Case 3 (Possion noise) | Case 3 (Possion noise) | Case 3 (Possion noise) | Case 3 (Possion noise) | Case 3 (Possion noise) | Case 3 (Possion noise)

Fig. 7. Spectral vector of one pixel and its denoising results in Pavia dataset. Case 1: Gaussian i.i.d. noise $\sigma = 0.1$. Case 2: Gaussian non-i.i.d. noise. Case 3: Poissonian noise.

TABLE IV
CLASSIFICATION ACCURACY RESULTS FOR INDIAN PINES

Method	Original	BM3D	DRUNet	HSID-CNN	NAILRMA	FastHyDe	Sub+DnCNN	Ours
OA	74.19%	76.62%	78.66%	80.50%	79.94%	79.67%	80.41%	**80.86%**
Kappa	0.7021	0.7306	0.7540	0.7773	0.7697	0.7657	0.7754	**0.7798**

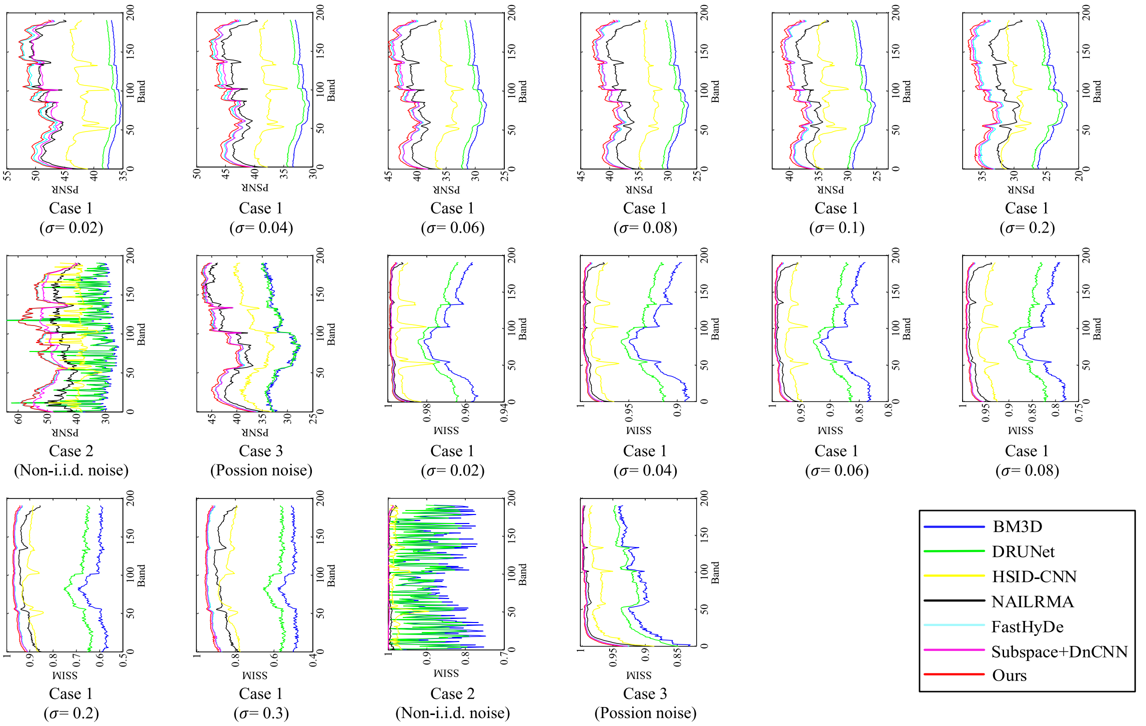

Case 1 (σ= 0.02) Case 1 (σ= 0.04) Case 1 (σ= 0.06) Case 1 (σ= 0.08) Case 1 (σ= 0.1) Case 1 (σ= 0.2) Case 1 (σ= 0.3)

Case 2 (Non-i.i.d. noise) Case 3 (Possion noise) Case 1 (σ= 0.02) Case 1 (σ= 0.04) Case 1 (σ= 0.06) Case 1 (σ= 0.08) Case 1 (σ= 0.1)

Case 1 (σ= 0.2) Case 1 (σ= 0.3) Case 2 (Non-i.i.d. noise) Case 3 (Possion noise)

Fig. 8. PSNR and SSIM values of each band of denoised dc Mall images. Case 1: Gaussian i.i.d. noise. Case 2: Gaussian non-i.i.d. noise. Case 3: Poissonian noise.

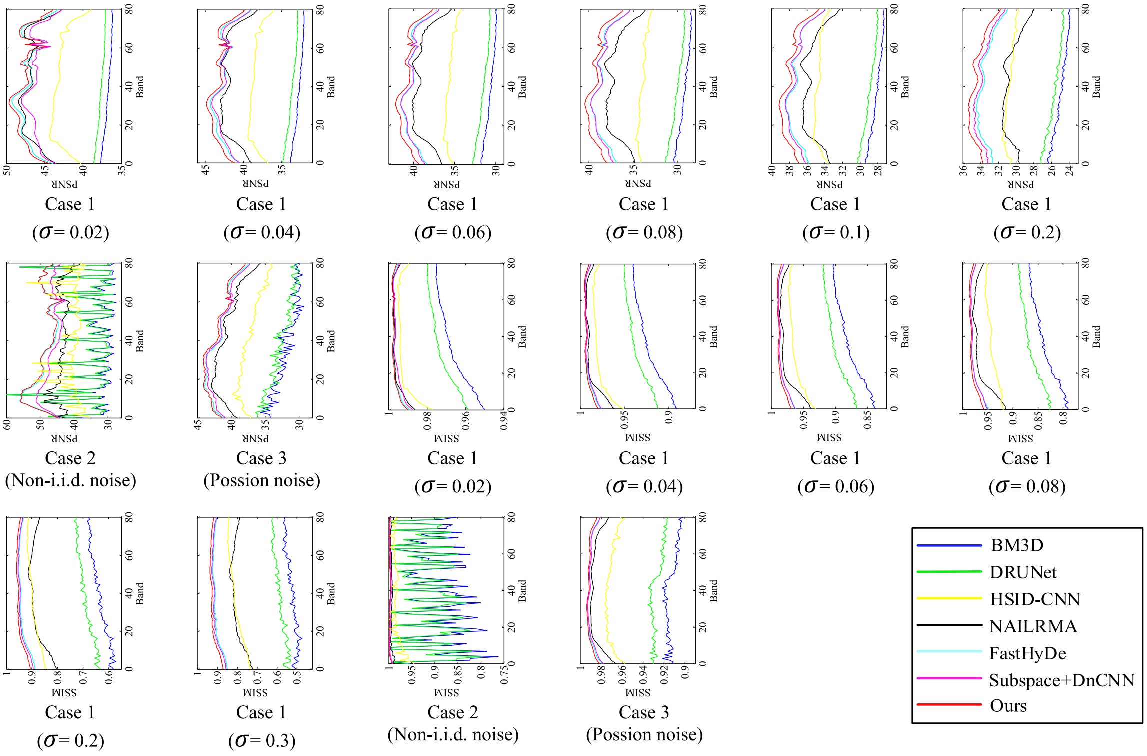

Case 1 (σ= 0.02) Case 1 (σ= 0.04) Case 1 (σ= 0.06) Case 1 (σ= 0.08) Case 1 (σ= 0.1) Case 1 (σ= 0.2) Case 1 (σ= 0.3)

Case 2 (Non-i.i.d. noise) Case 3 (Possion noise) Case 1 (σ= 0.02) Case 1 (σ= 0.04) Case 1 (σ= 0.06) Case 1 (σ= 0.08) Case 1 (σ= 0.1)

Case 1 (σ= 0.2) Case 1 (σ= 0.3) Case 2 (Non-i.i.d. noise) Case 3 (Possion noise)

Fig. 9. PSNR and SSIM values of each band of denoised Pavia images. Case 1: Gaussian i.i.d. noise. Case 2: Gaussian non-i.i.d. noise. Case 3: Poissonian noise.

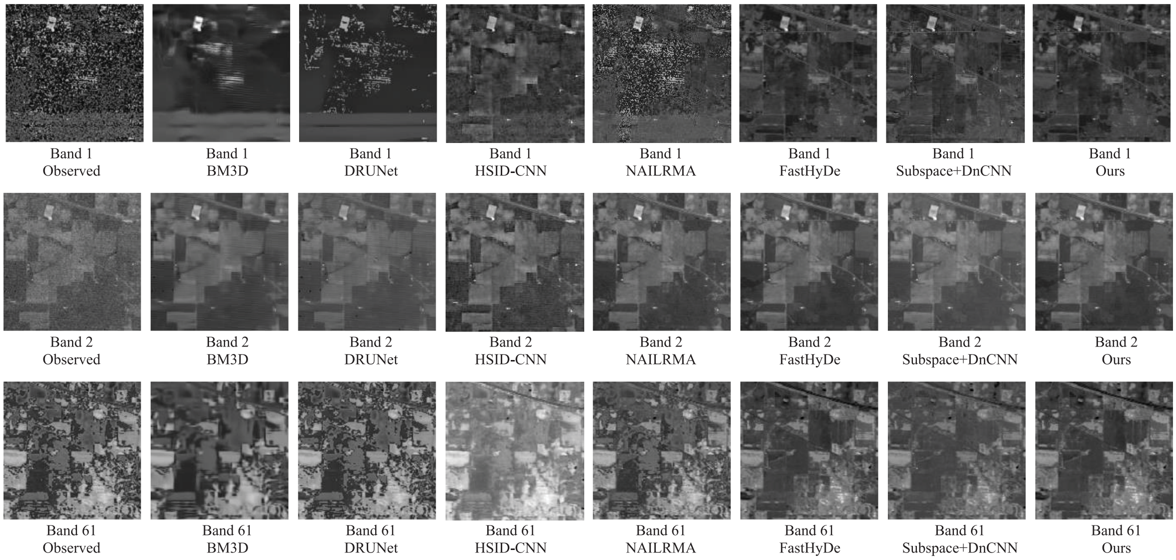

Band 1 Observed | Band 1 BM3D | Band 1 DRUNet | Band 1 HSID-CNN | Band 1 NAILRMA | Band 1 FastHyDe | Band 1 Subspace+DnCNN | Band 1 Ours

Band 2 Observed | Band 2 BM3D | Band 2 DRUNet | Band 2 HSID-CNN | Band 2 NAILRMA | Band 2 FastHyDe | Band 2 Subspace+DnCNN | Band 2 Ours

Band 61 Observed | Band 61 BM3D | Band 61 DRUNet | Band 61 HSID-CNN | Band 61 NAILRMA | Band 61 FastHyDe | Band 61 Subspace+DnCNN | Band 61 Ours

Fig. 10. Denoised results of different methods in Indian pines.

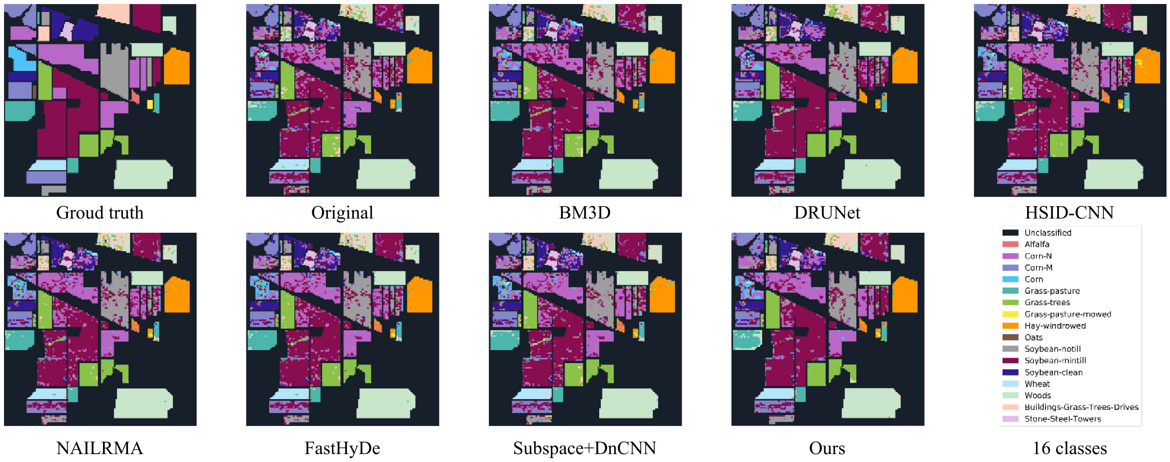

Groud truth | Original | BM3D | DRUNet | HSID-CNN

NAILRMA | FastHyDe | Subspace+DnCNN | Ours | 16 classes

Fig. 11. Classification results for the Indian pines images.

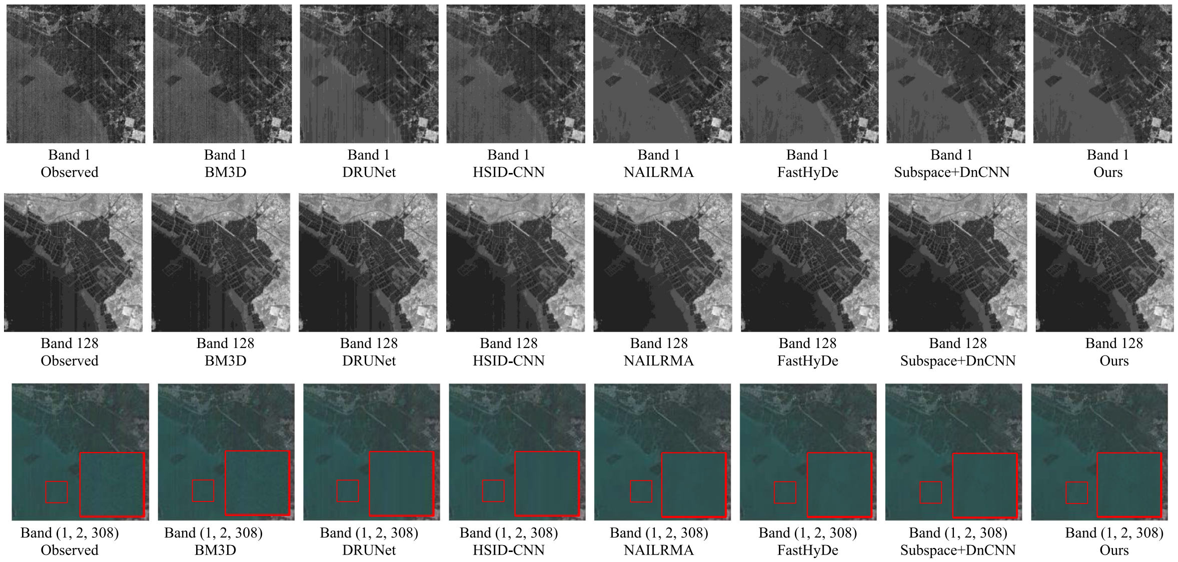

Band 1 Observed | Band 1 BM3D | Band 1 DRUNet | Band 1 HSID-CNN | Band 1 NAILRMA | Band 1 FastHyDe | Band 1 Subspace+DnCNN | Band 1 Ours

Band 128 Observed | Band 128 BM3D | Band 128 DRUNet | Band 128 HSID-CNN | Band 128 NAILRMA | Band 128 FastHyDe | Band 128 Subspace+DnCNN | Band 128 Ours

Band (1, 2, 308) Observed | Band (1, 2, 308) BM3D | Band (1, 2, 308) DRUNet | Band (1, 2, 308) HSID-CNN | Band (1, 2, 308) NAILRMA | Band (1, 2, 308) FastHyDe | Band (1, 2, 308) Subspace+DnCNN | Band (1, 2, 308) Ours

Fig. 12. Denoised results of different methods for GF-5 subregion image.

with 17 bands discarded. A subregion image of size 300×300 pixels was tested for our experiment.

The first column of Fig. 12 shows band 1, band 128 and the pseudocolor image with bands (1, 2, 308) separately, which all display strong noise and obvious stripes. Our method exhibits a good denoising effect. Although there are still rare and slight stripes in band 1, it retains more details than NAILRMA whose results display over smooth. For example, it can be seen from the zoomed area of pseudocolor images that our results preserved the "fishing ground" while denoising effectively.

V. CONCLUSION

In this article, we proposed a PnP framework to address HSI denoising task. A low-rank and sparse representation method is used to model the spatial–spectral low-rank prior of HSIs and derive subspace representation coefficients images (termed eigen-images), while eigen-images are denoised with CNN denoiser that is DRUNet. We embed them into the PnP framework to propose the PnP HSI denoising model with low-rank representation and CNN denoiser prior, which is user-friendly, requiring no retraining and utilizes the powerful performance of denoising CNN. Compared with other advanced denoising methods, the proposed method has better performance for both additive Gaussian noise and Poissonian noise. The simulated and real data experimental results also show that our model could more effectively maintain the details, the main structure and texture information of HSIs.

ACKNOWLEDGMENT

The authors would like to thank Prof. D. Landgrebe at Purdue University for providing the free downloads of the HYDICE image of the Washington DC Mall, and Jet Propulsion Laboratory for generously providing the airborne visible/ infrared imaging spectrometer data.

REFERENCES

[1] M. Weiss, F. Jacob, and G. Duveiller, "Remote sensing for agricultural applications: A meta-review," *Remote Sens. Environ.*, vol. 236, Jan. 2020, Art. no. 111402.

[2] T. Hu, W. Li, N. Liu, R. Tao, F. Zhang, and P. Scheunders, "Hyperspectral image restoration using adaptive anisotropy total variation and nuclear norms," *IEEE Trans. Geosci. Remote Sens.*, vol. 59, no. 2, pp. 1516–1533, Feb. 2021.

[3] P. Liu, H. Zhang, and K. B. Eom, "Active deep learning for classification of hyperspectral images," *IEEE J. Sel. Topics Appl. Earth Observ. Remote Sens.*, vol. 10, no. 2, pp. 712–724, Feb. 2017.

[4] L. Du *et al.*, "Application of hyperspectral LiDAR on 3-D chlorophyll-nitrogen mapping of Rohdea Japonica in laboratory," *IEEE J. Sel. Topics Appl. Earth Observ. Remote Sens.*, vol. 14, pp. 9667–9679, Sep. 2021.

[5] R. Pelta and E. Ben-Dor, "Assessing the detection limit of petroleum hydrocarbon in soils using hyperspectral remote-sensing," *Remote Sens. Environ.*, vol. 224, pp. 145–153, 2019.

[6] R. Tao, X. Zhao, W. Li, H.-C. Li, and Q. Du, "Hyperspectral anomaly detection by fractional fourier entropy," *IEEE J. Sel. Topics Appl. Earth Observ. Remote Sens.*, vol. 12, no. 12, pp. 4920–4929, Dec. 2019.

[7] Y. Wang, J. Peng, Q. Zhao, Y. Leung, X.-L. Zhao, and D. Meng, "Hyperspectral image restoration via total variation regularized low-rank tensor decomposition," *IEEE J. Sel. Topics Appl. Earth Observ. Remote Sens.*, vol. 11, no. 4, pp. 1227–1243, Apr. 2018.

[8] A. Buades, B. Coll, and J.-M. Morel, "A non-local algorithm for image denoising," in *Proc. IEEE Comput. Soc. Conf. Comput. Vis. Pattern Recognit.*, Jun. 2005, vol. 2, pp. 60–65.

[9] L. I. Rudin, S. Osher, and E. Fatemi, "Nonlinear total variation based noise removal algorithms," *Physica D*, vol. 60, no. 1, pp. 259–268, Nov. 1992.

[10] A. M. Teodoro, M. S. C. Almeida, and M. A. T. Figueiredo, "Single-frame image denoising and inpainting using gaussian mixtures," in *Proc. Int. Conf. Pattern Recognit. Appl. Methods*, 2015, pp. 283–288.

[11] S. Gu, L. Zhang, W. Zuo, and X. Feng, "Weighted nuclear norm minimization with application to image denoising," in *Proc. IEEE Conf. Comput. Vis. Pattern Recognit.*, 2014, pp. 2862–2869.

[12] K. Dabov, A. Foi, V. Katkovnik, and K. Egiazarian, "Image denoising by sparse 3-D transform-domain collaborative filtering," *IEEE Trans. Image Process.*, vol. 16, no. 8, pp. 2080–2095, Aug. 2007.

[13] T. Hu, W. Li, N. Liu, R. Tao, F. Zhang, and P. Scheunders, "Hyperspectral image restoration using adaptive anisotropy total variation and nuclear norms," *IEEE Trans. Geosci. Remote Sens.*, vol. 59, no. 2, pp. 1516–1533, Feb. 2021.

[14] Q. Yuan, L. Zhang, and H. Shen, "Hyperspectral image denoising employing a spectral–spatial adaptive total variation model," *IEEE Trans. Geosci. Remote Sens.*, vol. 50, no. 10, pp. 3660–3677, Oct. 2012.

[15] M. Maggioni, V. Katkovnik, K. Egiazarian, and A. Foi, "Nonlocal transform-domain filter for volumetric data denoising and reconstruction," *IEEE Trans. Image Process.*, vol. 22, no. 1, pp. 119–133, Jan. 2013.

[16] M. Maggioni, G. Boracchi, A. Foi, and K. Egiazarian, "Video denoising, deblocking, and enhancement through separable 4-D nonlocal spatiotemporal transforms," *IEEE Trans. Image Process.*, vol. 21, no. 9, pp. 3952–3966, Sep. 2012.

[17] A. Danielyan, A. Foi, V. Katkovnik, and K. Egiazarian, "Denoising of multispectral images via nonlocal groupwise Spectrum-PCA," *Conf. Colour Graph., Imag., Vis.*, vol. 2010, no. 1, pp. 261–266, 2010.

[18] J. Xu, L. Zhang, D. Zhang, and X. Feng, "Multi-channel weighted nuclear norm minimization for real color image denoising," in *Proc. IEEE Int. Conf. Comput. Vis.*, 2017, pp. 1096–1104.

[19] G. Chen, T. D. Bui, K. G. Quach, and S.-E. Qian, "Denoising hyperspectral imagery using principal component analysis and block-matching 4D filtering," *Can. J. Remote Sens.*, vol. 40, no. 1, pp. 60–66, Jan. 2014.

[20] J. Peng *et al.*, "Low-Rank and sparse representation for hyperspectral image processing: A review," *IEEE Geosci. Remote Sens. Mag.*, early access, Jun. 20, 2021, doi: 10.1109/MGRS.2021.3075491.

[21] M. Nejati, S. Samavi, S. M. Reza Soroushmehr, and K. Najarian, "Low-rank regularized collaborative filtering for image denoising," in *Proc. IEEE Int. Conf. Image Process.*, Sep. 2015, pp. 730–734.

[22] W. He, H. Zhang, L. Zhang, and H. Shen, "Hyperspectral image denoising via noise-adjusted iterative low-rank matrix approximation," *IEEE J. Sel. Topics Appl. Earth Observ. Remote Sens.*, vol. 8, no. 6, pp. 3050–3061, Jun. 2015.

[23] W. He, H. Zhang, L. Zhang, and H. Shen, "Total-variation-regularized low-rank matrix factorization for hyperspectral image restoration," *IEEE Trans. Geosci. Remote Sens.*, vol. 54, no. 1, pp. 178–188, Jan. 2016.

[24] L. Zhuang and J. M. Bioucas-Dias, "Fast hyperspectral image denoising and inpainting based on low-rank and sparse representations," *IEEE J. Sel. Topics Appl. Earth Observ. Remote Sens.*, vol. 11, no. 3, pp. 730–742, Mar. 2018.

[25] L. Zhuang, L. Gao, B. Zhang, X. Fu, and J. M. Bioucas-Dias, "Hyperspectral image denoising and anomaly detection based on low-rank and sparse representations," *IEEE Trans. Geosci. Remote Sens.*, vol. 60, pp. 1–17, 2020, Art. no. 5500117.

[26] Y. Chang, L. Yan, X.-L. Zhao, H. Fang, Z. Zhang, and S. Zhong, "Weighted low-rank tensor recovery for hyperspectral image restoration," *IEEE Trans. Cybern.*, vol. 50, no. 11, pp. 4558–4572, Nov. 2020.

[27] W. Sun, J. Peng, G. Yang, and Q. Du, "Fast and latent low-rank subspace clustering for hyperspectral band selection," *IEEE Trans. Geosci. Remote Sens.*, vol. 58, no. 6, pp. 3906–3915, Jun. 2020.

[28] L. Li, W. Li, Q. Du, and R. Tao, "Low-Rank and sparse decomposition with mixture of gaussian for hyperspectral anomaly detection," *IEEE Trans. Cybern.*, vol. 51, no. 9, pp. 4363–4372, Sep. 2021.

[29] Y. Qu, H. Qi, and C. Kwan, "Unsupervised sparse dirichlet-net for hyperspectral image super-resolution," in *Proc. IEEE Conf. Comput. Vis. Pattern Recognit.*, 2018, pp. 2511–2520.

[30] S. Cheng, Y. Wang, H. Huang, D. Liu, H. Fan, and S. Liu, "NBNet: Noise basis learning for image denoising with subspace projection," in *Proc. IEEE/CVF Conf. Comput. Vis. Pattern Recognit.*, 2021, pp. 4896–4906.

[31] W. Xie, X. Jia, Y. Li, and J. Lei, "Hyperspectral image super-resolution using deep feature matrix factorization," *IEEE Trans. Geosci. Remote Sens.*, vol. 57, no. 8, pp. 6055–6067, Aug. 2019.

[32] K. Zheng, L. Gao, Q. Ran, X. Cui, B. Zhang, and W. Liao, "Separable-spectral convolution and inception network for hyperspectral image super-resolution," *Int. J. Mach. Learn. Cybern.*, vol. 10, no. 10, pp. 2593–2607, 2019.

[33] X. Cao *et al.*, "Deformable image registration based on similarity-steered CNN regression," in *Proc. Med. Image Comput. Comput. Assist. Intervention*, 2017, pp. 300–308.

[34] D. Hong *et al.*, "More diverse means better: Multimodal deep learning meets remote-sensing imagery classification," *IEEE Trans. Geosci. Remote Sens.*, vol. 59, no. 5, pp. 4340–4354, May 2021.

[35] Y. Chang, L. Yan, H. Fang, S. Zhong, and W. Liao, "HSI-DeNet: Hyperspectral image restoration via convolutional neural network," *IEEE Trans. Geosci. Remote Sens.*, vol. 57, no. 2, pp. 667–682, Feb. 2019.

[36] K. Zhang, W. Zuo, Y. Chen, D. Meng, and L. Zhang, "Beyond a gaussian denoiser: Residual learning of deep CNN for image denoising," *IEEE Trans. Image Process.*, vol. 26, no. 7, pp. 3142–3155, Jul. 2017.

[37] K. Zhang, W. Zuo, and L. Zhang, "FFDNet: Toward a fast and flexible solution for CNN based image denoising," *IEEE Trans. Image Process.*, vol. 27, no. 9, pp. 4608–4622, 2018.

[38] Q. Zhang, Q. Yuan, J. Li, X. Liu, H. Shen, and L. Zhang, "Hybrid noise removal in hyperspectral imagery with a spatial–spectral gradient network," *IEEE Trans. Geosci. Remote Sens.*, vol. 57, no. 10, pp. 7317–7329, Oct. 2019.

[39] S. V. Venkatakrishnan and C. A. Bouman, "Plug-and-play priors for model-based reconstruction," in *Proc. IEEE Global Conf. Signal Inf. Process.*, 2013, pp. 945–948.

[40] K. Zhang, Y. Li, W. Zuo, L. Zhang, L. Van Gool, and R. Timofte, "Plug-and-Play image restoration with deep denoiser prior," *IEEE Trans. Pattern Anal. Mach. Intell.*, early access, Jun. 14, 2021, doi: 10.1109/TPAMI.2021.3088914.

[41] J. M. Bioucas-Dias *et al.*., "Hyperspectral unmixing overview: Geometrical, statistical, and sparse regression-based approaches," *IEEE J. Sel. Topics Appl. Earth Observ. Remote Sens.*, vol. 5, no. 2, pp. 354–379, Apr. 2012.

[42] M. Zhao, X. Wang, J. Chen, and W. Chen, "A plug-and-play priors framework for hyperspectral unmixing," *IEEE Trans. Geosci. Remote Sens.*, vol. 60, pp. 1–13, 2021, Art. no. 5501213.

[43] Y. Liu, X. Zhao, Y. Zheng, T. Ma, and H. Zhang, "Hyperspectral image restoration by tensor fibered rank constrained optimization and Plug-and-Play regularization," *IEEE Trans. Geosci. Remote Sens.*, vol. 60, pp. 1–17, 2021, Art. no. 5500717.

[44] X. Fu, S. Jia, L. Zhuang, M. Xu, and J. Zhou, "Hyperspectral anomaly detection via deep Plug-and-Play denoising CNN regularization," *IEEE Trans. Geosci. Remote Sens.*, vol. 59, no. 11, pp. 9553–9568, Nov. 2021. [Online]. Available: https://ieeexplore.ieee.org/abstract/document/9329138/

[45] X. Wang, M. Zhao, and J. Chen, "Hyperspectral unmixing via plug-and-play priors," in *Proc. IEEE Int. Conf.*, 2020, pp. 1063–1067. [Online]. Available: https://ieeexplore.ieee.org/abstract/document/9190817/

[46] H. Zeng, X. Xie, H. Cui, Y. Zhao, and J. Ning, "Hyperspectral image restoration via cnn denoiser prior regularized low-rank tensor recovery," *Comput. Vis. Image Underst.*, vol. 197–198, Aug. 2020, Art. no. 103004. [Online]. Available: https://www.sciencedirect.com/science/article/pii/S1077314220300710

[47] S. Boyd, N. Parikh, E. Chu, B. Peleato, and J. Eckstein, "Distributed optimization and statistical learning via the alternating direction method of multipliers," *Found. Trends Mach. Learn.*, vol. 3, no. 1, pp. 1–122, Jan. 2011.

[48] D. Geman and C. Yang, "Nonlinear image recovery with half-quadratic regularization," *IEEE Trans. Image Process.*, vol. 4, no. 7, pp. 932–946, Jul. 1995.

[49] A. Danielyan, V. Katkovnik, and K. Egiazarian, "Image deblurring by augmented lagrangian with BM3D frame prior," in *Proc. Workshop Inf. Theoretic Methods Sci. Eng.*, 2010, pp. 1–6.

[50] V. K. Danielyan and K. Egiazarian, "BM3D frames and variational image deblurring," *IEEE Trans. Image Process.*, vol. 21, no. 4, pp. 1715–1728, Apr. 2012.

[51] N. Yair and T. Michaeli, "Multi-scale weighted nuclear norm image restoration," in *Proc. IEEE Conf. Comput. Vis. Pattern Recognit.*, 2018, pp. 3165–3174.

[52] A. M. Teodoro, J. M. Bioucas-Dias, and M. A. T. Figueiredo, "Image restoration and reconstruction using variable splitting and class-adapted imagepriors,"in *Proc. IEEE Int. Conf. Image Process.*, Sep. 2016, pp. 3518–3522.

[53] K. Egiazarian and V. Katkovnik, "Single image super-resolution via BM3D sparse coding," in *Proc. 23rd Eur. Signal Process. Conf.*, 2015, pp. 2849–2853.

[54] A. M. Teodoro and J. M. Bioucas-Dias, "Block-Gaussian-mixture priors for hyperspectral denoising and inpainting," *IEEE Trans. Geosci. Remote Sens.*, vol. 59, no. 3, pp. 2478–2486, Mar. 2020.

[55] Y. Romano, M. Elad, and P. Milanfar, "The little engine that could: Regularization by denoising (RED)," *SIAM J. Imag. Sci.*, vol. 10, no. 4, pp. 1804–1844, 2017. [Online]. Available: https://epubs.siam.org/doi/abs/10.1137/16M1102884

[56] K. Zhang, W. Zuo, S. Gu, and L. Zhang, "Learning deep CNN denoiser prior for image restoration," in *Proc. IEEE Conf. Comput. Vis. Pattern Recognit.*, 2017, pp. 3929–3938.

[57] T. Tirer and R. Giryes, "Image restoration by iterative denoising and backward projections," *IEEE Trans. Image Process.*, vol. 28, no. 3, pp. 1220–1234, Mar. 2019.

[58] E. Ryu, J. Liu, S. Wang, X. Chen, Z. Wang, and W. Yin, "Plug-and-Play methods provably converge with properly trained denoisers," in *Proc. 36th Int. Conf. Mach. Learn.*, 2019, vol. 97, pp. 5546–5557.

[59] Y. Sun, J. Liu, and U. S. Kamilov, "Block coordinate regularization by denoising," May 13, 2019. [Online]. Available: http://arxiv.org/abs/1905.05113

[60] J. Bioucas-Dias and J. Nascimento, "Hyperspectral subspace identification," *IEEE Trans. Geosci. Remote Sens.*, vol. 46, no. 8, pp. 2435–2445, Aug. 2008.

[61] Q. Yuan *et al.*, "Hyperspectral image denoising employing a spatial–spectral deep residual convolutional neural network," *IEEE Trans. Geosci. Remote Sens.*, vol. 57, no. 2, pp. 1205–1218, Feb. 2018.

[62] L. Breiman, "Random forests," *Mach. Learn.*, vol. 45, no. 1, pp. 5–32, 2001.

Hezhi Sun received the B.S. degree in aircraft design and engineering and the M.S degree in aerospace science and technology from Harbin Institute of Technology, Harbin, China, in 2015 and 2018, respectively, where he is currently working toward the Ph.D. degree in aerospace science and technology with the School of Astronautics.

His research interests at that time included space electric propulsion and its applications. His current research interests include hyperspectral image processing, machine learning, deep learning, and their application in Earth Vision.

Ming Liu was born in Jilin Province, China, in 1981. He received the B.S. degree in information and computing Science, and the M.S. degree in operational research and cybernetics from the Northeastern University, Liaoning, China, in 2003 and 2006, respectively, and the Ph.D. degree in mathematics from the City University of Hong Kong, Hong Kong, in 2009.

In 2010, he was with Harbin Institute of Technology, where he is currently a Professor. His research interests include networked control systems, fault detection and fault tolerant control, and sliding mode control.

Dr. Liu was selected as the "New Century Excellent Talents in University" of the Ministry of Education of China in 2013 and the "Top-Notch Young Talents of Ten-Thousands Talents Program" in 2018.

Ke Zheng received B.S. degree in geographic information system from Shandong Agricultural University, Taian, China, in 2012, and the M.S. and Ph.D. degrees in remote sensing from the College of Geosciences and Surveying Engineering, China University of Mining and Technology (Beijing), Beijing, China, in 2016 and 2020, respectively.

Since 2020, he has been a Post-Doctoral Associate with the Key Laboratory of Digital Earth Science, Aerospace Information Research Institute, Chinese Academy of Science, Beijing, China. His research interests include image processing, machine learning, deep learning and their application in Earth Vision.

Dong Yang received the Ph.D. degree in optics from Jilin University, Changchun, China, in 2007.

He is currently with China Academy of Space Technology, Beijing, China.

Jindong Li received the Ph.D. degree in engineering thermophysics from Tsinghua University, Beijing, China, in 1992.

He is currently with China Academy of Space Technology, Beijing, China.

Lianru Gao (Senior Member, IEEE) received the B.S. degree in civil engineering from Tsinghua University, Beijing, China, in 2002, the Ph.D. degree in cartography and geographic information system from the Institute of Remote Sensing Applications, Chinese Academy of Sciences (CAS), Beijing, China, in 2007.

He is currently a Professor with the Key Laboratory of Digital Earth Science, Aerospace Information Research Institute, CAS. He also has been a visiting scholar at the University of Extremadura, Cáceres, Spain, in 2014, and with the Mississippi State University (MSU), Starkville, MS, USA, in 2016. In last ten years, he was the PI of ten scientific research projects at national and ministerial levels, including projects by the National Natural Science Foundation of China (2016–2019, 2018–2020, and 2022–2025), and by the Key Research Program of the CAS (2013–2015) He has authored or coauthored more than 180 peer-reviewed papers, and there are more than 100 journal papers included by Science Citation Index. He was coauthor of three academic books including “Hyperspectral Image Information Extraction”. He obtained 29 National Invention Patents in China. His research focuses on hyperspectral image processing and information extraction

Dr. Gao was the recipient of the Outstanding Science and Technology Achievement Prize of the CAS in 2016, and was supported by the China National Science Fund for Excellent Young Scholars in 2017, the Second Prize of The State Scientific and Technological Progress Award in 2018, the Best Reviewers of the IEEE JSTARS in 2015, and the Best Reviewers of the IEEE TGRS in 2017.